

The Stability of Radiatively Cooled Jets in Three Dimensions

Jianjun Xu¹

Department of Astronomy, The University of Maryland,
College Park, Maryland, MD 20742

Philip E. Hardee

Department of Physics & Astronomy, The University of Alabama,
Tuscaloosa, AL 35487; hardee@athena.astr.ua.edu

and

James M. Stone

Department of Astronomy, The University of Maryland,
College Park, Maryland, MD 20742; jstone@astro.umd.edu

Received March 2000 ; accepted June 2000 to appear ApJ, 543, November 10

arXiv:astro-ph/0007446v1 28 Jul 2000

¹IMS, MCIWorldcom, Vienna, VA 22182

ABSTRACT

The effect of optically thin radiative cooling on the Kelvin-Helmholtz instability of three dimensional jets is investigated via linear stability theory and nonlinear hydrodynamical simulation. Two different cooling functions are considered: radiative cooling is found to have a significant effect on the stability of the jet in each case. The wavelengths and growth rates of unstable modes in the numerical simulations are found to be in good agreement with theoretical predictions. Disruption of the jet is found to be sensitive to the precessional frequency at the origin with lower frequencies leading to more rapid disruption. Strong nonlinear effects are observed as the result of the large number of normal modes in three dimensions which provide rich mode-mode interactions. These mode-mode interactions provide new mechanisms for the formation of knots in the flows. Significant structural features found in the numerical simulations appear similar to structures observed on protostellar jets.

Subject headings: galaxies: jets — hydrodynamics — instabilities — ISM: jets and outflows

1. Introduction

High resolution imaging surveys have revealed the association between Herbig-Haro (HH) objects and protostellar jets (Reipurth et al. 1986; Strom et al. 1986; Mundt et al. 1987; Ray 1987). Although individual HH objects can be formed via different mechanisms, most HH objects appear as bright knots along collimated jets, or associated with the working surface at the head of the jet, e.g., HH 46/47 (Graham & Elias 1983), HH 40 (Mundt et al. 1984), HH 34 (Bührke, Mundt, & Ray 1988), and HH 111 (Reipurth et al. 1997). Recent HST observations of HH 111 (Reipurth et al. 1997) indicate that the bright knots along the jet beam arise from “bow” shocks associated with dense knots inside a collimated outflow. Sinusoidal distortion of the jet in HH 111 and staggering of the “bow” shocks suggest that the jet beam is helically twisted. HST observations of HH 30 (Burrows et al. 1996) also reveal bright knots inside the jet beam. The proper motion of these knots has been detected and the observed bending of the jet changes with time, again suggesting helical twisting of the jet beam.

A supersonic astrophysical jet is Kelvin-Helmholtz (K-H) unstable [see Birkinshaw (1991) for a review], and complex structures can be formed through the growth of instabilities in the jet beam. The study of the stability of supersonic astrophysical jets has focused on two fundamental questions: (1) What is required to make jets sufficiently stable to propagate large distances (up to a pc in the case of protostellar jets and hundreds of Kpc in extragalactic sources), and (2) what emission features, e.g., individual HH objects, are formed through instabilities in the jet beam? In protostellar jets, optically thin radiative cooling can strongly affect the dynamics, e.g., Blondin et al. (1990), Stone & Norman (1993a, 1993b, 1994), de Gouveia dal Pino & Benz (1993). These earliest numerical studies focused on propagation of the jets and interactions at the jet front, and showed that radiative cooling yielded strong fragmentation in a dense shell of material swept up by the working surface at the jet head.

Interactions behind the jet front and the development of knots in a jet beam were first considered by Falle et al. (1987) who proposed that standing shocks could form the knots. Subsequently the knots were observed to have large proper motions (e.g. Eislöffel & Mundt 1995), and to have a close spacing inconsistent with standing shocks in the high Mach number flows. Later work showed that pulsation (temporal variation) of the outflow at the 10% level could produce aligned knots with bow shock morphology, e.g., Reipurth et al. (1986), Raga & Kofman (1992), Stone & Norman (1993b) de Gouveia Dal Pino & Benz (1994); Biro & Raga (1994); Biro (1996); Suttner et al. (1997). It was also suggested that knots can be the result of K-H flow instability, e.g., Bührke, Mundt, & Ray (1988), Ray & Mundt (1993), Bodo et al. (1994), Rossi et al. (1997); Downes & Ray (1998). Additionally, the K-H instability could produce helically twisted structural features. That asymmetric structural features could be produced by K-H instability is suggested by recent 2D linear stability analysis and 2D numerical simulations (Hardee & Stone 1997; Stone, Xu, & Hardee 1997). This work showed that radiative cooling can increase the growth rate of K-H unstable modes significantly, and revealed a variety of asymmetric structural features formed as a result of instability.

In this paper we study the K-H instability of 3D radiatively cooling jets through a systematic comparison between numerical simulations and linear stability theory over a wide parameter range. In §2 we describe the protostellar environment and radiative cooling assumed in this study. In §3 the 3D linear stability theory is summarized, and representative normal mode solutions appropriate to the numerical simulations are obtained. The numerical simulation results are shown in §4. In §4.2 we consider development of the surface wave modes and in §4.3 we consider development of the body wave modes and wave-wave interaction, and the pressure and velocity fluctuations arising from wave-wave interactions are compared to computations made from the

linear theory. Our numerical results are summarized in §5 and in §6 structures seen in the simulated jets are compared with observed protostellar jet structures.

2. The Protostellar Jet Environment

Protostellar jets show the same type of spectrum as low excitation HH objects, and the dominant emission lines include [S II] and the Balmer lines. The spectra are best explained as originating from a radiative shock, with velocity in the range 30 – 60 km s⁻¹ (Ray 1997). Although there are some YSO jets that contain high excitation emission, this emission can usually be identified with strong bow shocks where portions of the jet are moving into the ambient medium with a velocity of a few hundreds of km s⁻¹, comparable to the typical velocities of ~ 200 km s⁻¹ exhibited by the fastest moving knots in the jet beam. The emission line spectra observed in typical YSO jets indicates that temperatures in the radiatively cooling regions are $3 \times 10^4 - 10^5$ K, and line ratios, e.g., [S II] $\lambda = 6716\text{\AA}$ & 6731\AA , suggest that electron densities are $N_e \sim 100 - 10,000$ cm⁻³ in the radiatively cooling regions.

In addition to observational evidence that protostellar jets are overdense with respect to their surroundings (e.g., Ray 1997), results from numerical studies have shown that a propagating jet creates a cocoon behind the bow shock filled with hot gas that is less dense than the jet. Dense molecular outflows which are often observed to be associated with protostellar jets (Reipurth & Cernicharo 1995) may surround the cocoon. The kinematic model of a dense jet embedded in a less dense cocoon which is in turn ensheathed by a very dense and cold molecular gas is consistent with detailed observation of a number of systems, e.g., HH 111 whose jet is surrounded by a bubble within the larger molecular outflow (Nagar et al. 1997; Cernicharo & Reipurth 1996). Since we focus our study on the stability properties of the jet beam which is only influenced by the jet’s immediate surroundings, we can model a protostellar jet as a dense jet beam embedded in a hotter and less dense cocoon. In particular, we will assume that the protostellar jet is surrounded by a uniform, optically thin medium with low density (typically ~ 100 cm⁻³) and high temperature (typically $\gtrsim 10^4$ K). The fact that protostellar jets remain well collimated for lengths which are much larger than their radii argues they must be in pressure equilibrium with their surroundings. Numerical studies also have shown that the jet beam remains cold, neutral, and in approximate pressure balance with the cocoon medium. Pressure balance implies a jet temperature of $T_{jt} = (n_{ex}/n_{jt})T_{ex}$, where the subscripts *ex* and *jt* denote the external cocoon and jet gas respectively. Observations of some HH jets (Bührke, Mundt, & Ray 1988) indicate that typically the internal jet density exceeds the cocoon density by at least a factor of 10. For $T_{ex} \sim 10^4$ K and $n_{jt}/n_{ex} = 10$, $T_{jt} \sim 10^3$ K. This indicates that the linear analysis of the equilibrium jet can focus on cooling processes which are effective with jet temperatures $\sim 10^3$ K and cocoon temperatures $\gtrsim 10^4$ K. Because shocks with $v_s \sim 100$ km s⁻¹ give temperatures as high as 10^6 K, temperatures higher than 10^6 K are considered in the cooling function in the numerical simulations.

Optical emission from a protostellar jet and from the external gas results in a loss of internal energy from the system, and the loss of internal energy through radiative cooling can change the jet dynamics substantially. Thus, an important aspect of the numerical simulation of radiatively cooling jets is an accurate treatment of the microphysical heating and cooling rates. While it has been shown that a non-equilibrium ionization formalism significantly improves the accuracy of cooling terms (Stone & Norman 1993a), incorporating a time-dependent ionization fraction into a linear stability analysis is intractable. Thus, the cooling rate is assumed to be given by equilibrium cooling curves. In the work to follow two separate cooling curves are adopted: (1) the cooling curve for interstellar gas appropriate to protostellar jets calculated by Dalgarno & McCray (1972, hereafter DM), or (2) the curve described by MacDonald & Bailey (1981, hereafter MB) for

photoionized gas of reduced metallicity such as that found in elliptical galaxies and appropriate to extragalactic jets. While not strictly applicable to protostellar jets, the MB cooling curve allows us to explore the effect of temperature dependence of the cooling curve on jet dynamics. The full DM and MB cooling curves used in the simulations along with the piecewise power-law fits used in the linear analysis can be found in Figure 1 of Hardee & Stone (1997).

3. The Linear Theory

3.1. Normal Mode Analysis

The stability of an adiabatic 3D jet with “top hat” profile residing in a uniform medium has been thoroughly investigated in the literature (see Birkinshaw 1991). Modifications to the adiabatic 3D theory to account for radiative cooling are identical to those found in the 2D theory (Hardee & Stone 1997) and we sketch the results here. The hydrodynamic equations of continuity, momentum, and energy are linearized within the jet and the external (cocoon) gas where $\mathbf{u} = 0$ and the flow velocity is reintroduced when solutions are matched at the jet boundary. The linearized hydrodynamical equations relevant to our model become

$$\frac{\partial \rho_1}{\partial t} + \nabla \cdot (\rho_0 \mathbf{v}_1) = 0, \quad (1)$$

$$\frac{\partial \mathbf{v}_1}{\partial t} = -\frac{1}{\rho_0} \nabla P_1, \quad (2)$$

$$\frac{\partial}{\partial t} P_1 + F_p P_1 = \Gamma \frac{P_0}{\rho_0} \left(\frac{\partial}{\partial t} \rho_1 + F_p \rho_1 \right), \quad (3)$$

where, in general, the perturbed quantities are written as $\rho = \rho_0 + \rho_1$, $\mathbf{v} = \mathbf{u} + \mathbf{v}_1$, and $P = P_0 + P_1$. The energy equation is written following Hunter & Whitaker (1989) with

$$F_p = \frac{\Gamma(\Gamma - 1)}{\rho_0 a^2} C_0 \left(\left. \frac{\partial \ln C}{\partial \ln T} \right|_{\rho} - \left. \frac{\partial \ln H}{\partial \ln T} \right|_{\rho} \right),$$

and

$$F_p = \frac{\Gamma - 1}{\rho_0 a^2} C_0 \left(\left. \frac{\partial \ln C}{\partial \ln T} \right|_{\rho} - \left. \frac{\partial \ln C}{\partial \ln \rho} \right|_T + \left. \frac{\partial \ln H}{\partial \ln \rho} \right|_T - \left. \frac{\partial \ln H}{\partial \ln T} \right|_{\rho} \right),$$

where C_0 is the initial cooling rate, $a \equiv (\Gamma P_0 / \rho_0)^{1/2}$ is the sound speed, and Γ is the adiabatic index.

In cylindrical geometry a random perturbation of ρ_1 , \mathbf{v}_1 , and P_1 to an initial equilibrium state ρ_0 , \mathbf{u} , and P_0 can be considered to consist of Fourier components of the form

$$f_1(r, \phi, z) = f_1(r) \exp[i(kz \pm n\phi - \omega t)] \quad (4)$$

where flow is along the z -axis, and r is in the radial direction with the flow bounded by $r = R$. In cylindrical geometry k is the longitudinal wavenumber, n is an integer azimuthal wavenumber, for $n > 0$ the wavefronts are at an angle to the flow direction, the angle of the wavevector relative to the flow direction is $\theta = \tan(n/kR)$, and $+n$ and $-n$ refer to wave propagation in the clockwise and counterclockwise sense, respectively, when viewed outwards along the flow direction. In equation (4) $n = 0, 1, 2, 3, 4$, etc. correspond to pinching, helical, elliptical, triangular, rectangular, etc.

normal mode distortions of the jet, respectively. Propagation and growth or damping of the Fourier components is described by a dispersion relation

$$\frac{\beta_{jt} J'_n(\beta_{jt} R_{jt})}{\chi_{jt} J_n(\beta_{jt} R_{jt})} = \frac{\beta_{ex} H'_n(\beta_{ex} R_{jt})}{\chi_{ex} H_n(\beta_{ex} R_{jt})}, \quad (5)$$

where the primes denote derivatives of the Bessel (J) and Hankel (H) functions with respect to their arguments, β and χ are given by

$$\beta_{ex} = [-k^2 + \frac{\omega^2}{a_{ex}^2} Q_{ex}]^{1/2},$$

$$\beta_{jt} = [-k^2 + \frac{(\omega - ku)^2}{a_{jt}^2} Q_{jt}]^{1/2},$$

and

$$\chi_{ex} = \rho_{ex} \omega^2,$$

$$\chi_{jt} = \rho_{jt} (\omega - ku)^2.$$

All heating and cooling information is contained in the dimensionless terms Q_{jt} and Q_{ex} where

$$Q_{ex} = \frac{1 + iF_p^{ex}/\omega}{1 + iF_\rho^{ex}/\omega},$$

and

$$Q_{jt} = \frac{1 + iF_p^{jt}/(\omega - ku)}{1 + iF_\rho^{jt}/(\omega - ku)}.$$

For normal mode n the axial wavelength associated with a 360° helical twist of a wavefront around the jet beam is given by $\lambda_z = n\lambda_n$ where $\lambda_n = 2\pi/k$. The angular frequency appearing in the linear analysis, ω , represents a $360^\circ/n$ helical twist and is properly related to an angular precession frequency by $\omega = n\omega_p$. For example, if an elliptical jet distortion, normal mode $n = 2$, rotates 360° with the precession frequency ω_p , at a fixed azimuthal angle the frequency at which the jet surface oscillates is $2\omega_p$. In general, each normal mode, n , consists of a single “surface” wave and multiple “body” wave solutions to the dispersion relation. Structural differences between the surface and body waves are discussed in §3.4.

3.2. Heating and Cooling Rates

Following previous 2D work (Hardee & Stone 1997; Stone, Xu, & Hardee 1997), we chose a jet of radius $R_{jt} = 2.5 \times 10^{15}$ cm with number density $n_{jt} = 600 \text{ cm}^{-3}$, temperature $T_{jt} = 10^3$ K and sound speed $a_{jt} = 3.73 \times 10^5 \text{ cm s}^{-1}$. Initially the jet is in pressure equilibrium with an external (cocoon) gas with number density $n_{ex} = 60 \text{ cm}^{-3}$, temperature $T_{ex} = 10^4$ K and sound speed $a_{ex} = 1.18 \times 10^6 \text{ cm s}^{-1}$. With heating and cooling rates of the form $H = \Lambda_H n^{\alpha_H} T^{\beta_H}$, and $C = \Lambda_C n^{\alpha_C} T^{\beta_C}$, F_p and F_ρ are given by

$$F_p = \frac{\Gamma(\Gamma - 1)}{\rho_0 a^2} \mathbf{C}(\beta_C - \beta_H),$$

and

$$F_\rho = \frac{\Gamma - 1}{\rho_0 a^2} \mathbf{C} [(\beta_C - \beta_H) + (\alpha_H - \alpha_C)],$$

where $\mathbf{C} = \Lambda_C n_0^{\alpha_C} T_0^{\beta_C}$ ergs cm⁻³ s⁻¹. We will assume that the heating rate is independent of the temperature, i.e., $\beta_H = 0$, and is proportional to the density, i.e., $\alpha_H = 1$, and the initial equilibrium requires that $H_0 = C_0$.

In the linear analysis a piecewise power-law fit to the DM cooling function is represented by

$$\Lambda_{DM} = \begin{cases} 3.0 \times 10^{-28} T^{0.5} \text{ erg cm}^3 \text{ s}^{-1} & : T < 10^4 \text{ K} \\ 1.5 \times 10^{-24} T^{0.5} \text{ erg cm}^3 \text{ s}^{-1} & : T \geq 10^4 \text{ K} \end{cases}$$

For DM cooling, $\mathbf{C} = \Lambda_C n_0^{\alpha_C} T_0^{\beta_C} = n_0^2 \Lambda_{DM}$ and for our choice of parameters

$$\begin{Bmatrix} F_p^{ex} \\ F_p^{jt} \end{Bmatrix} = \frac{5}{9\rho_0 a^2} \Lambda_C n_0^2 T_0^{0.5} = \begin{Bmatrix} 2.16 \times 10^{-9} \text{ s}^{-1} \\ 1.37 \times 10^{-11} \text{ s}^{-1} \end{Bmatrix},$$

and

$$\begin{Bmatrix} F_\rho^{ex} \\ F_\rho^{jt} \end{Bmatrix} = -\frac{1}{3\rho_0 a^2} \Lambda_C n_0^2 T_0^{0.5} = \begin{Bmatrix} -1.29 \times 10^{-9} \text{ s}^{-1} \\ -0.82 \times 10^{-11} \text{ s}^{-1} \end{Bmatrix}.$$

A power-law fit to MB cooling curve of the form

$$\Lambda_{MB} = 1.5 \times 10^{-34} T^{2.53} \text{ erg cm}^3 \text{ s}^{-1}$$

is used in the linear analysis to simulate the MB cooling curve. For MB cooling, $\mathbf{C} = \Lambda_C n_0^{\alpha_C} T_0^{\beta_C} = n_0^2 \Lambda_{MB}$ and for our choice of parameters

$$\begin{Bmatrix} F_p^{ex} \\ F_p^{jt} \end{Bmatrix} \approx \frac{25}{9\rho_0 a^2} \Lambda_C n_0^2 T_0^{2.53} = \begin{Bmatrix} 1.46 \times 10^{-10} \text{ s}^{-1} \\ 4.30 \times 10^{-11} \text{ s}^{-1} \end{Bmatrix},$$

and

$$\begin{Bmatrix} F_\rho^{ex} \\ F_\rho^{jt} \end{Bmatrix} \approx \frac{1}{\rho_0 a^2} \Lambda_C n_0^2 T_0^{2.53} = \begin{Bmatrix} 5.24 \times 10^{-11} \text{ s}^{-1} \\ 1.54 \times 10^{-11} \text{ s}^{-1} \end{Bmatrix}.$$

The most important difference in jet stability properties between DM cooling and MB cooling arises from the change in sign of F_ρ (Hardee & Stone 1997). The positive value of F_ρ for MB cooling is a consequence of the steeper temperature dependence of the MB cooling function. Positive values of F_ρ occur when $(\beta_C - \beta_H) + (\alpha_H - \alpha_C) > 0$. For our choice of heating rate depending linearly on the density and of cooling rate depending on the density squared, $F_\rho > 0$ when $\beta_C > 1$. The DM power-law fit used in the linear analysis serves to illustrate the effect of a shallow dependence of radiative cooling on temperature in both jet and external fluid. The MB power-law fit used in the linear theory serves to illustrate the effect of a steep dependence of radiative cooling on temperature in both jet and external fluid. In the simulations and in the theory the “equilibrium” heating rate $H_0 = C_0$ is determined by the requirement that the jet and external medium be in thermal equilibrium initially. Because cooling rates are different in the jet and external fluids as a result of temperature and density differences, the initial heating rate required to establish and maintain thermal equilibrium is different in the two fluids.

3.3. Dispersion Relation Solutions

Numerical solutions to the dispersion relation for adiabatic (AD), Dalgarno & McCray (DM) cooling and MacDonald & Bailey (MB) cooling jets have been obtained for the pinch, helical, elliptical, triangular and rectangular normal modes for $M_{ex} \equiv u/a_{ex} = 5$ and 20 jets, jet speeds of 59 km s^{-1} and 236 km s^{-1} , respectively. The solutions for $M_{ex} \equiv u/a_{ex} = 5$ and 20 are qualitatively similar, and in Figure 1 we show those appropriate to $M_{ex} = 20$ and a jet speed of 236 km s^{-1} . In the numerical simulations, and possibly in protostellar systems, jets are perturbed at their origin by a periodic motion at some frequency; thus, we solve the dispersion relation for a complex wavenumber as a function of angular frequency. A negative value for the imaginary part of the wavenumber indicates spatial growth at that angular frequency with an e-folding length $\ell_e = |k_I^{-1}|$.

We identify the following features in the 3D solutions:

(1) The solutions for the pinch and helical normal modes in 3D are very similar to the solutions obtained in 2D for the symmetric (pinch) and asymmetric (sinusoidal) normal modes of the slab jet (Hardee & Stone 1997). The higher order normal modes of the 3D jet which have no analog on the 2D jet, e.g., the elliptical etc. normal modes, can be thought of as harmonics of the helical mode and behave similarly to helical mode solutions.

(2) In general, the linear growth rates, $|k_I|$, scale inversely with the Mach number (not shown), and the linear growth rates, especially for the body modes, are relatively smaller in 3D than in 2D. Body wave mode growth rates can be larger, comparable to or smaller than the growth rate of the surface wave mode for the pinch, helical and elliptical normal modes, respectively. Body wave mode growth rates are less than the surface wave modes for all higher order normal modes (not shown).

(3) The effect of radiative cooling on the dispersion relation is similar in 2D and 3D, i.e., DM cooling significantly increases the linear growth rate at higher frequencies and MB cooling decreases the linear growth rate at higher frequencies. The high frequency growth rate plateau for DM cooling extends to frequencies only slightly higher than those shown in the figure, at which point the growth rate rapidly declines towards the adiabatic results at high frequency. Adiabatic and MB cooling jets show distinct “resonant” (fastest growing) angular frequencies, ω^* , and wavelengths, λ^* , for almost all surface and body wave solutions, and the DM cooling jet shows distinct resonances for the body wave solutions. As was found in 2D the presence of DM cooling adds a pinch cooling mode (Ps2) that does not exist for AD or MB cooling jets. In general, the wave modes are purely real on the adiabatic jet or damped on the radiatively cooling jets (damping rates not shown) in regions where they are not growing.

3.4. Fluid Displacements, Velocity & Pressure Fluctuations

Displacements, $\xi(r, \phi, z)$, of jet fluid from an initial position (r, ϕ, z) can be written in the form

$$\xi(r_0, \phi_s, z_s) = \mathbf{A}(r_0)e^{i\Delta(r_0)}\xi_r(R) \exp[i(kz_s \pm n\phi_s - \omega t)] , \quad (6)$$

where z_s and ϕ_s are the axial and azimuthal positions at the jet surface, r_0 is the initial radial position, $\xi_r(R)$ is the radial displacement at the jet surface, the $\mathbf{A}(r)e^{i\Delta(r)}$ are given by equations (A10) in Hardee, Clarke, & Rosen (1997, hereafter HCR), and the $k(\omega)$ are normal mode solutions to the dispersion relation. Fluid displacements are modified in amplitude and rotated in azimuthal angle or shifted along the jet axis relative to those at the jet surface by $\mathbf{A}(r)e^{i\Delta(r)}$. The difference

in structure between surface and body wave solutions on adiabatic jets at their resonant frequencies as revealed by displacement surfaces is shown explicitly by Figure 13 in HCR. The accompanying velocity perturbation, $\mathbf{v}_1(r, \phi, z) = d\boldsymbol{\xi}/dt$, and pressure perturbation, $P_1(r, \phi, z)$, can be written in the form

$$\mathbf{v}_1(r', \phi', z') = -i(\omega - ku)\mathbf{A}(r_0)e^{i\Delta(r_0)}\xi_r(R)\exp[i(kz_s \pm n\phi_s - \omega t)] , \quad (7)$$

$$P_1(r', \phi', z') = B(r_0)e^{i\Delta_p(r_0)}\xi_r(R)\exp[i(kz_s \pm n\phi_s - \omega t)] , \quad (8)$$

where points on initially cylindrical surfaces are displaced radially to $r' = r_0 + \delta r$, axially to $z' = z_s + \delta z$, and azimuthally to $\phi' = \phi_s + \delta\phi$, and δr , δz , $\delta\phi$ are the components of $\boldsymbol{\xi}(r_0, \phi_s, z_s)$. In equation (8) $B(r_0)e^{i\Delta_p(r_0)} = (\chi_{jt}/\beta_{jt})[J_n(\beta_{jt}r_0)/J'_n(\beta_{jt}R)]$ [e.g., Hardee et al. 1998 eq. (14)]. The total velocity is given by $\mathbf{v} = \mathbf{u} + \mathbf{v}_1$ and the total pressure is given by $P = P_0 + P_1$.

If the azimuthal and axial phase shift is small then the radial fluid displacement of a “surface” wave mode $n > 0$ in the jet interior at constant azimuthal angle is $\xi_r(r) \approx \xi_r(R)(r/R)^{n-1}$ (Hardee 1983). The accompanying velocity and pressure variations produced by higher order surface modes also show a rapid decrease inwards. On the other hand, at a constant azimuth the “body” wave modes have a reversal in fluid displacement at “null displacement” surfaces in the jet interior and typically the maximum pressure is near the null surface.

Jet distortion and accompanying pressure and velocity structure associated with individual normal mode surface and body waves at frequencies less than or equal to the resonant frequency have been thoroughly investigated for adiabatic flows (Hardee et al. 1998; Hardee 2000). Jet distortion and the accompanying pressure and velocity structure across the jet and parallel to the jet axis are not strongly modified by radiative cooling and the structure of the individual wave modes on adiabatic and cooling jets as a function of frequency at and below the resonant frequency of the appropriate mode is similar. The numerical simulations presented in the next several sections perturb the jets at low frequencies and at high frequencies above the resonant frequency. At the higher frequencies the simulations reveal interesting wave-wave interactions that have not been investigated previously. We will consider the high frequency structure of various modes in comparison with structures observed in the numerical simulations in §4.3.

4. Numerical Simulations

4.1. Initial and Boundary Conditions

All of the simulations were performed using the modified three-dimensional hydrodynamic code CMHOG. For details on the hydrodynamical algorithms see Stone, Xu, & Hardee (1997). At dimensionless simulation time $\tau_{sim} \equiv (a_{ex}/R_{jt})t = 0$, a jet beam of Mach number M_{ex} with uniform density n_{jt} and z -velocity $u_z = M_{ex}a_{ex}$ is set up across a Cartesian computational grid in the z direction. Outflow boundary conditions are used except where the jet enters the computational grid where inflow boundary conditions are used. The size of the computational domain is varied in the axial direction depending on the Mach number of the jet and the perturbation frequency in order to ensure that many wavelengths of the most unstable mode are captured. Simulations with DM and MB type cooling were performed, along with simulations of adiabatic jets (AD) that serve as a baseline for comparison. Grid size along with all the other key parameters associated with the simulations are listed in Table 1. Note that the duration of various simulations, τ_{sim} , is different.

In these simulations we study the dynamical evolution of unstable jets that are initially in a delicate pressure equilibrium with a low-density ambient medium and in which the gas is

established in thermal equilibrium with net cooling rate $n^2\Lambda - nH = 0$. To maintain thermal equilibrium a different heating rate, H , is used in jet and ambient fluid and the initial equilibrium could be maintained for many dynamical times if the system was not perturbed. As the perturbed simulations evolve and the fluids mix the heating rate, H , is varied according to whether a grid zone temperature is above or below 10,000 K for DM cooling or according to the fraction of ambient and jet material in a grid zone for MB cooling. These different approaches reflect the discontinuity in the DM cooling function at 10,000 K and the continuity of the MB cooling function, and are identical to the methods used in the previous 2D simulations. The per particle cooling rate, Λ , is computed in each grid zone according to the complete DM or MB cooling curves (see Figure 1 in Stone, Xu, & Hardee 1997). Note that the net cooling rate is now non-zero but is less than $n^2\Lambda$. As a result the cooling length $\ell_{cool} > v_{shock}t_{cool} \sim v_{jt}t_{cool}$ where $t_{cool} \equiv (\Gamma - 1)^{-1}(kT/n\Lambda)$, and shocked regions in the ambient medium can be underresolved with cooling length a few times the grid spacing. However, underresolution of these shocks does not influence the stability or internal structure of the jet beam which is primarily what we study here.

A periodic precession of the jet velocity is applied at the jet nozzle to break the symmetry. In the simulations, the pitch angle, θ , of the jet velocity relative to the axial direction varies from $\theta = 0.0025$ to 0.01 rad depending on the precession frequency. As in previous 2D simulations (Stone, Xu, & Hardee 1997) we choose the initial precession (perturbation) frequency to be $\omega R_{jt}/u = 0.1$, 0.4 and 1.0 for Mach 5 jets, and $\omega R_{jt}/u = 0.025$ and 1.0 for Mach 20 jets. With our assumed jet radius and velocities the precession period ranges from about 840 to 21 years.

4.2. Surface Wave Modes

4.2.1. Low Frequency Precession

We performed simulations with angular frequency $\omega R_{jt}/u = 0.1$ and $\omega R_{jt}/u = 0.025$ on Mach 5 and 20 jets, respectively. This angular frequency is about a factor of three below the resonant frequency on the AD jet, and for our assumed jet radius and flow speeds corresponds to a precession period $\tau_p = 843.7$ yr. Mach 20 jets have speeds that are comparable to observed protostellar jets. As comparable behavior is seen in the Mach 5 and 20 numerical simulations, albeit with different length scale we show a volumetric rendering of the density for Mach 20 AD and DM jets in Figure 2. At precession frequencies much below the AD helical resonance, the linear theory indicates that helical and higher order surface wave modes will be dominant as the surface mode growth rates are much higher than the body mode growth rates on AD jets and body modes are damped on DM and MB jets at this low precession frequency (see Figure 1).

The dominant oscillation is the result of helical twisting excited by the precession at the inlet. Note that the Mach 20 AD jet remains collimated across most of the computational grid even though the linear growth rates of AD and DM jets are nearly the same at this low precession frequency. Thus, non-linear processes speed the breakup of radiatively cooling jets relative to adiabatic jets. A similar result was found in 2D for identical parameters (see Figure 9 in Stone, Xu, & Hardee 1997). Some high density knot formation is apparent in the region where the Mach 20 DM jet breaks up at a distance slightly less than $400R_{jt}$, approximately 2.3 e-folding lengths. A 2D DM jet breaks up at a slightly longer distance at this precession frequency even though the 2D sinusoidal surface mode growth rate is larger than the 3D helical surface mode growth rate (about 50% larger). Upon break up the 2D jet develops denser knots. We note that the Mach 5 DM jet develops similarly but only propagates about 1/4 the distance of the Mach 20 jet – about $100R_{jt}$ at break up. This difference is about the factor indicated by the direct scaling between growth length and Mach number predicted from theoretically computed spatial growth rates. Very

little knot formation occurs at the lower speed of the Mach 5 jet in 2D or in 3D simulations.

In the region where Mach 20 and Mach 5 DM jets break up the structure is very complicated and bow shocks are the dominant feature. This region also shows rapid mixing of jet and ambient material. The mixing, as measured by an entrainment volume and by an entrained mass, for the Mach 5 DM simulation as a function of position along the jet beam at time $\tau_{sim} = 100$ is shown in Figure 3. The entrainment volume V_ϵ is defined as that volume of the fluid that has $C > \epsilon$ where $0 < \epsilon < 1$ (e.g., Loken et al. 1996), and C is a “color” variable that traces the jet fluid. A value $V_\epsilon = 1$ indicates that all zones on the grid in a plane transverse to the jet axis at location z contain jet material with $C > \epsilon$. The entrained mass M_δ is defined as the mass of fluid with an axial velocity $v_z > \delta a_{ex}$ (e.g., Loken et al. 1996; Bassett & Woodward 1995). Mixing is considerably enhanced in 3D relative to a similar 2D Mach 5 numerical simulation (see Figure 11 in Stone, Xu, & Hardee 1997). The volume containing entrained material saturates near $z = 50R_{jt}$ in 3D versus $300R_{jt}$ in 2D. This is due to the dramatic increase in area of the jet ambient medium interface when the 3D jet disrupts, thus accelerating the mixing process. The entrained mass shows an increase only for axial velocities of jet and entrained material that are less than the external sound speed, i.e., $\delta < 1$, whereas in 2D the entrained mass showed an increase for $\delta \leq 2$. This is a result of the fast break-up and rapid slow down of jet material accompanying the mixing process in 3D. Note that the decline in entrained volume and mass at axial distances $z > 125R_{jt}$ has occurred as flow from the inlet no longer reaches these distances at time $\tau_{sim} = 100$. Presumably the slowly moving mixed material would progress across the computational grid at longer times.

4.2.2. Moderate Frequency Precession

In the Mach 5 simulations the angular precession frequency $\omega R_{jt}/u = 0.4$ is on the order of the resonant frequency of the first few normal mode “surface” waves on the AD and MB jets, and is within the unstable frequency range for the important accompanying “body” waves on AD, DM, and MB jets. For our assumed jet radius and flow speed this angular frequency corresponds to a precession period of $\tau_p = 210.9$ yr. No comparable simulations were performed for Mach 20 jets. The jets showed helical twisting at wavelengths, $\lambda/R_{jt} \sim 14.3$ (AD), 15.6 (DM), and 14.3 (MB), very close to those predicted theoretically – 14.1 (AD), 15.6 (DM) and 14.0 (MB) – where theoretical wavelengths are given by $\lambda/R_{jt} = 2\pi v_{gp}/\omega$ and $v_{gp} \equiv (\partial\omega/\partial k)|_{real}$ is the group velocity at the precession frequency. Thus, the linear analysis correctly predicts the helical wavelengths.

At this precession frequency the surface modes all have substantial growth rates. Ultimately, growth of these modes can cause the jet to bifurcate or trifurcate. Splitting the jet into filaments provides a large interface between the jet and ambient medium, and the observed rapid mixing with the external medium. Quantitative comparison between linear growth rates shown in Table 2 indicates that the linear growth rate for the helical surface mode is smallest for the adiabatic jet, larger for the MB cooling jet, and largest for the DM cooling jet. At least qualitatively, the more rapid predicted growth of helical instability on the cooling jets is verified by the simulations. The rapid growth of higher order surface modes (see §4.2.4) in 3D precludes a quantitative analysis of amplitude growth of the helical mode. In any event, at a moderate precession frequency, radiative cooling has accelerated the breakup of the jet beam, just as we found at a low precession frequency.

Outside the jet beam the simulations show a pattern of spiral shocks produced by the large amplitude helical twist. In the external gas this shock, when viewed edge on, appears as alternate bow-shaped arcs on each side of the jet beam. This is illustrated in Figure 4 by a volumetric rendering of the temperature and of the density from the Mach 5 DM simulation. High temperatures lie immediately behind the shock front, and the volumetric rendering of the

density shows that the shocks originate at dense knots on the jet surface. In Figure 5, we show a volumetric rendering of $\rho^2 T$ (density squared times temperature) for this Mach 5 DM cooling jet. The $\rho^2 T$ image emphasizes regions in the jet beam where the jet material is shocked and raised to higher temperatures and simulates emission from a single line, e.g., [S II]. At this frequency, the helical ridge on the surface of the jet beam is caused by the helical surface wave. The “hot spots” are caused by projection combined with “limb brightening”. The high temperature postshock gas behind the spiral shock forms a thin continuous radiating layer. If observed from a direction which is perpendicular to the jet beam, the radiative region looks like discrete “knots”. At larger distances the jet starts to entrain ambient material and dense knots are formed via cooling. These knots have a velocity slightly less than the initial jet velocity and a temperature which is much higher than the initial jet temperature.

4.2.3. High Frequency Precession

The precession frequency $\omega R_{jt}/u = 1.0$, about three times the helical resonant frequency on the Mach 5 adiabatic jet, corresponds to a precession period of $\tau_p = 84.4$ yr for our assumed jet radius and flow speed. Figure 6 shows the jet density in a slice plane along the jet axis for AD, DM, and MB Mach 5 jets at this frequency. No comparable simulations were performed for Mach 20 jets. The jet beams do not show a large amplitude helical twist, but the internal patterns reveal the presence of periodic knots inside the AD and DM jet beam. This result is similar to numerical simulations in 2D slab geometry (Norman & Hardee 1988; Hardee, Cooper, & Clarke 1994; Stone, Xu, & Hardee 1997) which have shown that the jet beam cannot respond bodily to perturbations much higher than the resonant frequency, i.e., the entire jet beam cannot form high frequency sinusoidal or helical patterns with significant surface displacement.

While these jets do not exhibit a large scale helical twist associated with the surface wave at the precession frequency, the presence of a resonant wavelength in the AD and MB jets is exhibited by a helical twist seen in the AD and MB simulations as the jets break up. In particular, we measure a helical twist in AD and MB simulations with wavelength $\lambda \approx 15R_{jt} \pm 2R_{jt}$. The linear theory predicts a resonant wavelength for the helical surface wave of $\lambda^* = 16.9R_{jt}$ and $13.2R_{jt}$ for AD and MB jets, respectively, in good agreement with the simulations. Thus, jet breakup is associated with helical twisting at about the resonant wavelength. These jets remain well collimated to distances in excess of double that associated with the moderate precession frequency that was near to the helical surface wave resonance. Thus, the collimation of the jets is preserved fairly well due to the inability of jet beams to respond bodily to the high precession frequency and very small perturbation at the lower resonant frequency.

4.2.4. Higher Order Surface Modes

Even though the precession that we use preferentially excites the helical surface mode, the higher order surface modes have higher maximum growth rates on AD, DM, and MB jets (see Figure 1) and can grow to significant amplitudes. Growth of the higher order modes is observed to lead to elliptical, triangular, rectangular, etc. distortions of the jet cross section in AD, DM, and MB Mach 5 jet simulations. This type of distortion is seen in all Mach 5 simulations performed with precession frequencies $\omega R_{jt}/u = 0.4$ & 1.0 . The lower of these two precession frequencies is at about the calculated resonant frequency for the helical through rectangular surface modes on AD and MB Mach 5 jets, is slightly below the high frequency growth rate plateau on the DM jet, and should excite these surface modes at about their maximum growth rates. The higher precession frequency lies in the range where body modes have their maximum growth rates and where the

surface modes have smaller growth rates and (or for the DM jet with high frequency surface mode growth rate plateau) have a lesser effect on jet distortion.

The development of cross section distortion from the Mach 5 DM simulation with precession frequency $\omega R_{jt}/u = 0.4$ is shown in Figure 7. Qualitatively similar results are found for the comparable Mach 5 AD and MB simulations. As first observed by Hardee & Clarke (1995), we find that higher order modes with the fastest growth rates appear first, and as one moves down the jet beam away from the nozzle, the cross section area of the jet first becomes pentagonal, then rectangular, triangular, and finally elliptical. Note the jet beam bifurcation as a result of the growth of the elliptical mode. Quantitatively, the distance where we expect to see the higher order modes to appear will be proportional to $\ell_e^* = |k_I^*|^{-1}$ where k_I^* is the maximum spatial growth rate. With our small amplitude initial perturbation, growth to a significant amplitude should require a distance of about $2\pi/k_I^*$, i.e., about six e-folding lengths, and these distances are listed in Table 2. We find that rectangular, triangular, and elliptical distortions appear in the same order along AD, DM and MB jets, and the locations of their appearance are close to the values listed in Table 2. Thus, the linear analysis correctly predicts the relative growth rates of the surface modes.

At a precession frequency of $\omega R_{jt}/u = 1.0$, the Mach 5 AD, DM and MB jets remain well collimated to about twice the distance of their $\omega R_{jt}/u = 0.4$ brethren. Cross sections (not shown) reveal lesser surface distortion but with internal structure consistent with the development of body modes. Thus, high frequency precession, where the linear analysis predicts that surface mode growth is reduced and/or perturbs only a shallow surface layer of the jet beam, is shown by the numerical simulations to be much less destabilizing to the jet beam than lower frequency precession as surface modes are suppressed.

4.3. The Body Modes & Wave-Wave Interactions

4.3.1. Low Frequency Precession

At precession frequencies much below the AD helical resonance, the linear theory indicates that helical and higher order surface wave modes will be dominant, and the body wave modes are either purely real on the AD jet or are damped on the DM and MB cooling jets. While growth may occur for all modes near resonance, the absence of initial perturbations at higher frequencies suggests that growth of the surface and/or body wave modes at resonance will be slow. In fact we find evidence for interaction between the helical surface wave and a weakly damped helical body wave where both are excited by the precessional perturbation.

An interaction between helical surface and body waves is shown in Figure 8, which contains composite volumetric renderings of $\rho^2 T$ from the Mach 5 DM cooling jet perturbed at a frequency of $\omega R_{jt}/u = 0.1$. The top panel shows the entire jet beam. The middle panel shows “hot spots” in the jet beam by excluding jet material with temperatures at or below 1,000 K. The bottom panel shows an enlargement of the knot region. The hot spots have temperatures ranging from 1000 K – 10,000 K and appear very prominently at locations of $z \approx 23$ & $37 R_{jt}$. However, at the precessional frequency the helical and higher order surface modes, have a wavelength of about $58 R_{jt}$ (from the linear analysis). Note the long wavelength oscillation evident in the images. On the other hand, the helical body modes are only weakly damped at this frequency with damping length $\sim 1000 R_{jt}$. If the helical surface wave with wavelength $\lambda_{surf} = 58.0 R_{jt}$, and the first helical body wave with wavelength $\lambda_{body} = 18.47 R_{jt}$ are in phase at the origin, subsequent in phase locations should occur at $23 R_{jt}$ and at $35.7 R_{jt}$. These positions are very close to the observed positions of the prominent knots at $z \approx 23$ & $37 R_{jt}$. The interaction can also be seen in jet cross

sections (not shown). Thus, the interaction between body waves and surface waves can lead to knot formation. Knots or hot spots created in this fashion are stationary.

A second type of interaction also appears possible. In the Mach 20 DM jet perturbed with a precessional frequency of $\omega R_{jt}/u = 0.025$ the jet ambient medium interface appears to break up at several locations (see Figure 2 and compare the Mach 20 AD and DM jets in the first half of the computational grid). The break up of the jet-ambient medium interface in this simulation appears to be the result of energy deposition at the jet surface from a damped internal body wave. With the exception of this feature the Mach 20 DM jet shows very little structure or evidence for dense knot formation inside the jet beam.

4.3.2. Moderate to High Frequency Precession

The angular frequencies $\omega R_{jt}/u = 0.4$ & 1.0 are within the unstable frequency range for the important “body” waves on AD, DM, and MB Mach 5 jets. In the DM and MB simulations at the lower frequency, we observe dense filaments aligned with jet flow inside the jet beam near to the surface, and see indications of dense knot formation. The location and length of these dense filaments is coincident with constructive wave-wave interactions between the first three helical body waves if all waves are launched from the origin in phase. For example, density cuts in a slice plane along the jet axis from the DM and MB simulations (not shown) reveal a dense filament of length $\sim 4.1R_{jt}$ at $z \leq 10R_{jt}$. We note that full wavelengths of the first, second and third helical body waves are $\lambda^*/R_{jt} = 10.1, 7.5$ and 6.0 , and the first helical body wave at $z = 10R_{jt}$ has over-run the third helical body wave by a distance of $\sim 4.1R_{jt}$ with less over-run for the second helical body wave. This suggests that compression over this length interior to $z = 10R_{jt}$ by the three body modes has led to radiative cooling and the observed filament formation.

At the higher angular frequency of $\omega R_{jt}/u = 1.0$ density cuts in a slice plane along the jet axis shown in Figure 6, and plots of pressure, axial and transverse velocities along the jet axis, shown in Figure 9 for the DM jet, reveal knot structure in the Mach 5 AD and DM jets with periodic spacing of $34.0R_{jt}$ and $27.6R_{jt}$, respectively. Similar structure is not seen on the MB jet. While the structure suggests periodic pinching and knot formation, the periodic spacing is much longer than the wavelength of any normal mode body or surface wave at the precession frequency. However, close examination of “resonant” wavenumbers for first and second helical body modes (Table 3) reveals a potential beat pattern with spacing of $39.2R_{jt}$ and $26.2R_{jt}$ for AD and DM jets, respectively, in excellent agreement with the observed knot spacing. The lack of a beat pattern and knots in the MB jet might be due to the low growth rate of the second body wave relative to the first body wave on the MB jet.

How can periodic knots be produced by a beat pattern between helical body modes? Since only the beat pattern between the two helical body modes can generate the observed wavelength, we interpret the simulation results to mean that the wave-wave interaction between the helical body waves has excited and funneled energy into a pinch mode at the long beat wavelength. To show how this could be so we have computed the pressure and velocity fluctuations accompanying the first two helical body modes, Hb1 and Hb2 using solutions computed from the dispersion relation for the Mach 5 DM jet at the precession frequency $\omega R/u = 1$, the fluctuations resulting from their beat pattern (Hb12), and the fluctuations associated with the pinch surface cooling mode Ps2 at the beat wavelength. Fluctuations were computed using equations 6 – 8 in §3.4. The results for pressure fluctuations appropriate to those observed in the Mach 5 DM simulation (Figure 9) are shown in Figure 10. In Figure 10 we plot component structure along 1D cuts parallel to the jet axis (z -axis) at different locations on the transverse $+y$ -axis where velocity

components v_x and v_y represent azimuthal and radial velocities, respectively. Coarse mapping of values computed in cylindrical (r, ϕ, z) coordinates to the Cartesian (x, y, z) coordinate location of the 1D cuts has led to the raggedness of the lines in the figure.

The 1D cuts are shown at multiple radial locations between jet center (dotted lines) and surface (dashed lines) for the first (Hb1) and second (Hb2) helical body waves. The highest pressures associated with Hb1 at this frequency are near the jet surface. The v_y (radial) velocity component shows opposing motions between material near the jet surface and in the jet interior, and a half-wavelength axial phase shift between outwards radial motion near the jet surface and at the jet center. The highest pressures associated with Hb2 are in the jet interior with a half-wavelength axial phase shift in pressure extrema between the jet surface and the jet center. At this frequency the radial velocity shows a large axial phase shift between jet surface and jet center. The axial velocity fluctuation is small for both helical body modes near jet center. The combination of the two helical body waves (Hb12) leads to a combined fluid displacement different from that of the individual waves, and the resulting pressure and velocity fluctuations along the jet axis (dotted lines) for the individual waves cannot simply be added to give the pressure fluctuation (dash-dotted line) and beat pattern in the transverse velocity components along the jet axis. Still the difference between the wavenumbers of the first and second helical body modes (see Table 3) leads to the beat pattern with wavelength of $\sim 26R_{jt}$. The transverse velocity components along the axis (dashed line & dotted line) are 90° out of phase as expected for helical distortion. Note the lack of fluctuation in the axial velocity component as is observed in the simulation. Pressure and velocity fluctuation structure resulting from this wave-wave interaction changes significantly off the jet axis.

The pressure and velocity fluctuations expected to accompany the pinch cooling mode (Ps2) between the jet axis and surface (dash-dotted line) at a wavelength comparable to the beat pattern between the two helical body mode waves and with a comparable pressure fluctuation shows a substantial axial velocity fluctuation and a lack of radial velocity fluctuation along the jet axis (dotted line) as is observed in the simulation. Pressure and axial velocity fluctuation do not change as a function of the radius but radial velocity fluctuation increases slightly towards the jet surface (dashed line). Clearly wave-wave interaction between the helical body modes couples via the pressure fluctuation near jet center to the pinch cooling mode with pressure fluctuation occupying a large fraction of the jet interior and with some non-linear interaction between the velocity components that results in both small axial and transverse velocity fluctuation near jet center. The resulting nearly axisymmetric periodic pressure and density fluctuation produces the observed knots.

4.3.3. *Very High Frequency Precession*

In the Mach 20 DM simulation we study jet response to an angular precession frequency of $\omega R_{jt}/u = 1.0$ that is over ten times the AD jet helical resonant frequency. For our assumed jet radius and flow speed this angular frequency corresponds to a precession period of $\tau_p = 21.1$ yr. At this frequency, the linear theory indicates a high frequency plateau in the surface wave mode growth rate that is above the body wave mode growth rates (see Figure 1). The helical nature of the initial precession guarantees that modes higher than helical are unlikely to develop to significant amplitude, although growth rates are comparable. We note that the wavelengths predicted to accompany this precession frequency are shorter for the helical surface mode than for helical body modes. This is a reversal of the usual relationship.

This simulation provides another interesting example of knot formation via wave-wave

interaction. Knot formation appears in the $\rho^2 T$ volumetric rendering image in the upper panel in Figure 11 at $\tau_{sim} = 5$. The volumetric rendering reveals a clear helical pattern within the jet beam with wavelength $6.5R_{jt}$. From the linear analysis, we calculate wavelengths of $\lambda_h = 4.8R_{jt}$, $6.65R_{jt}$, $6.31R_{jt}$, and $6.05R_{jt}$ for the helical surface and first three helical body modes, respectively, at the precession frequency. Thus, we tentatively identify the dominant pattern with the first helical body wave and the “hot spots” (at $z \sim 20$ & $35 R_{jt}$ in Figure 11) in the helical pattern as caused by wave-wave interaction between the helical surface wave and the first helical body wave as illustrated qualitatively by the lower panel in Figure 11. Additional information concerning wave-wave interactions is provided by profiles of pressure, axial velocity, and transverse velocity components along the z -axis shown in Figure 12. These profiles reveal that the transverse velocity components undergo out of phase sinusoidal oscillation (indicating helical twisting at jet center) which dies away and then returns at $z \sim 55R_{jt}$. The difference between the wavenumbers of the first and second helical body modes (see Table 3) can lead to a beat pattern with wavelength of $\sim 120R_{jt}$ similar to that revealed in Figure 12. While the pressure and axial velocity remain constant out to $z = 25R_{jt}$, Figure 12 shows the development of quasi-periodic pressure and axial velocity oscillation with an observed wavelength $\sim 6.7R_{jt}$ at larger distance that can only be produced by the second pinch body mode.

We show that the hot spots can be fit by interaction between the helical surface (Hs) and first helical body (Hb1) waves, and that the structure at jet center can be fit by a beat pattern between first (Hb1) and second (Hb2) helical body modes combined with the presence of the second pinch body mode (Pb2) in Figure 13. In Figure 13 fluctuations were computed using equations 6 – 8 in §3.4. Component structure is shown along 1D cuts parallel to the jet axis (z -axis) at different locations on the transverse $+y$ -axis where velocity components v_x and v_y represent azimuthal and radial velocities, respectively, like Figure 10. The pressure and velocity fluctuations that would accompany the helical surface (Hs), first body (Hb1) and second body (Hb2) waves using solutions computed from the dispersion relation for the Mach 20 DM jet at the precession frequency $\omega R/u = 1$ are shown. This frequency is above the resonant frequency for both body modes and lies on the high growth rate plateau for the surface mode wave. The axial phase shift in pressure and radial velocity fluctuations between jet center and surface for Hb1 is much smaller than that shown in Figure 10 for the Mach 5 solution. The difference is entirely the result of the difference in the frequency relative to the resonant frequency for this body mode. The axial phase shift in pressure and velocity fluctuation between jet center and surface for Hb2 is similar to that shown in Figure 10 for the Mach 5 solution. Note that significant pressure and velocity fluctuations associated with the surface wave occur only near to the jet surface (dashed line). Thus, the surface wave does not influence the jet interior at this high frequency. This result supports the conclusion that at high frequencies the helical surface wave mode can effect only a shallow layer near to the jet surface (Hardee & Norman 1988; Hardee & Stone 1997), whereas the body waves can still effect a larger volume of the jet beam.

Figure 13 also shows the result of wave-wave interaction between the surface and first two helical body modes (Hsb12). The beat wavelength (best illustrated by the transverse velocity fluctuations along the jet axis) is comparable to that seen in the simulation. Additionally, the figure shows the pressure fluctuation at the jet surface (dashed line) associated with the wave-wave interaction between the surface and first two helical body modes. Here we note an additional beat wavelength that arises between the surface and body modes near the jet surface, where the pressure fluctuations achieve maxima at axial distances $z/R \approx 20, 42$ and 65 . This confirms the tentative identification of the hot spots in the simulation with interaction between surface and body helical waves. Note that the beat wavelength shows a slow pressure variation along the jet axis (dotted line). A rise in the pressure along the axis occurs as the transverse (v_x, v_y) velocity fluctuations decrease. This behavior is identical to that seen in the body mode wave-wave

interaction (Hb12) shown in Figure 10. There is a small accompanying axial velocity variation on the axis. Just off the axis a short wavelength pressure and axial velocity fluctuation (solid line) is evident. This short wavelength fluctuation can couple to the pressure and velocity fluctuation expected to accompany the second pinch body mode (Pb2) to produce the short wavelength quasi-periodic pressure and axial velocity oscillation seen in the simulation with an observed wavelength $\sim 6.7R_{jt}$. Thus the simulation results again show that a wave-wave interaction between helical body modes can excite a pinch mode.

5. Summary

5.1. Comparison with theory

We have found that the analytical linear analysis provides both good qualitative and quantitative agreement with our 3D simulations. The linear analysis successfully indicates: (1) the dominate modes in various perturbation frequency ranges, (2) the increase in instability due to cooling, and (3) the frequency range in which mode-mode coupling is most likely to occur. Quantitative measurements of parameters such as the wavelengths of individual modes and the beat patterns formed by wave-wave interaction are correctly predicted and the order of occurrence of higher order surface modes are also matched quantitatively with the predictions from the linear analysis. In addition, velocity and pressure fluctuations computed from the theory appear to be in good quantitative agreement with fluctuations observed in the numerical simulations. The coupling between normal wave modes that we have found here has also been found in numerical simulations using a spectral type code by Keppens & Tóth (1999) who also have identified analytically the quasi-linear coupling mechanism that connects a driven helical mode to several other low order normal modes.

5.2. Disruption of the jet beam

3D simulations confirm results and conclusions reached in 2D simulations (Stone, Xu, & Hardee 1997). Cooling (especially DM type cooling) increases the linear growth rate of unstable modes, especially the helical surface and body modes, and helps to break up the jet beam particularly at perturbation frequencies at or below resonance relative to the adiabatic jet. What is unique in 3D is that higher order K-H modes play important roles in the jet evolution, filamentation and disruption. Animations of our 3D simulations and Figures 2, 5, 6 and 7 show that disruption of the jet beam can be categorized by two different fundamental processes: (1) the amplitude of distortion caused by helical and other low order surface wave modes grows large and the jet beam breaks into filaments in the direction of jet flow. The increase in the contact area between the jet beam and the ambient gas leads to enhanced mixing and leading edge shock and knot formation, and (2) the compression wave front established inside the jet by the initial perturbation is not reflected back into the jet beam from the jet-ambient interface but deposits energy at the jet surface and opens a gap in the jet surface, e.g., by a damped helical body mode. The gap creates a shock in the ambient gas, and the jet is disrupted.

It is clear that development of jet distortion, knot formation and jet disruption depend on the radiative cooling rate and the perturbation frequency. When the development of jet distortion is slowed, by whatever process, disruption is delayed. In general, radiative cooling speeds those processes leading to jet disruption relative to an adiabatic jet. DM cooling with a relatively shallow dependence of radiative cooling on temperature in both jet and external fluid is somewhat

more destabilizing than MB cooling with a steep dependence of radiative cooling on temperature in both jet and external fluid. Jets perturbed at high frequency even though helical surface and body modes have large growth rates are relatively stable to disruption. It is the value of the perturbation frequency relative to the resonant frequency and not the absolute value that is important. Typically, our jets remained collimated to twice the distance when perturbed at a high frequency when compared to jets perturbed at the resonant or lower perturbation frequency.

5.3. Knots & Shock Spurs

We note that knots in the present 3D simulations were less dense than in comparable 2D simulations. Mode-mode interactions, also present in 2D simulations, are more complicated in 3D. The interactions, such as helical surface and helical body mode interaction and coupling to pinch modes, lead to new mechanisms for the formation of staggered emission knots along the jet beam which can lead to staggered bow shocks or lead to relatively stationary knots in the jet beam.

(1) Shocks outside the jet beam created by large amplitude surface displacement provide one mechanism for knot formation and for the formation of shock spurs. In this case, the jet-ambient interface creates a spiral shaped shock around the jet beam in the ambient gas. If viewed edge-on, this shock presents a staggered pattern of shock spurs down the jet beam. Interior to the jet surface a strong density enhancement near the surface of the jet beam provided by large amplitude helical surface displacement accompanies the spiral shaped shock. Viewed edge-on the density enhancement looks like localized knots at the base of the shock spurs. These knots and shock spurs move with the speed of the helical surface wave.

(2) Wave-wave interactions provide a second mechanism for knot formation. In general, our results indicate some suppression of knot formation at low precession frequencies resulting from the absence of multiple body waves and the associated wave-wave interactions. In wave-wave interactions, the knots are formed internal to the jet beam and in one simulation the knots are seen to be stationary in temporal animations. Thus, no knot driven shocks are created in the ambient gas. Note that the material moving through the stationary knots is moving at nearly the jet speed and large radial velocities could still be observed from the spectral lines. However, in another simulation the knots formed as a result of wave-wave interaction near to the inlet are initially nearly stationary, but at larger distance the knots move and develop shock spurs. At high frequencies surface distortion leading to shock spurs does not occur.

(3) As a jet breaks up mixing with the external environment leads to shocks and knot formation. Knots formed in this fashion are primarily associated with the bow-shock region at the head of a protostellar jet. In our simulations this region moves outwards into an already outwards moving region where jet material previously existed. As a result the resulting bow shock is weaker than might be the case otherwise.

6. Discussion

Internal knots are one of the most prominent features of YSO jets. Knots have been seen to form at the source and move outwards with time, e.g., HH 80/81 (Marti et al. 1995) and the Serpens Radio Jets (Curiel 1995). Since they bear many of the same spectral signatures as individual HH objects, they should be related to radiative shocks. In our study, all the initial perturbations are chosen to be fairly small so as not to excite nonlinear dynamic effects. As a result, while we see complex internal structures we do not see strong shocks internal to the jet

beam as long as the jet is not disrupted. Bührke, Mundt, & Ray (1988) and Bodo et al. (1994) have proposed that the K-H pinch instability may cause knots to form in the jet beam. Our simulations do provide evidence for knots produced by pinching at wavelengths induced by helical wave-wave interaction. In our simulations the knots formed at the beat wavelength typically have negligible proper motion. There are pulsating jet models (see Stone & Norman 1993b and references therein) in which strong internal shocks are created in the jet beam. Knots created by the pulsating jet will have proper motions that are comparable to the jet speed.

Evidence for small and/or accelerating knot proper motion is provided by detailed emission line observations of HH 83 by Reipurth (1989). In this highly collimated jet there are about ten emission knots, and the jet terminates at a strong bow shock. The distance to the source is 460 pc (the source is in the Orion Cloud), and the inclination angle of the jet is $\sim 45^\circ$. Thus, the physical extent of the jet is about 0.1 pc. From the observed width of the brightest knots, the physical length-to-width ratio is at least 17. Therefore, from the source to the terminating bow shock the linear scale is at least $30R_{jt}$. Detailed spectral studies reveal that there is a systematic increase of the velocity from knot A to knots I and J from -80 km s^{-1} to -180 km s^{-1} , and the bow shock has H_α line emission only, which indicates a shock with velocity of 80 km s^{-1} or greater.

These observational results may be compared to our numerical simulation of a Mach 5 DM cooling jet (jet speed of about 60 km s^{-1}) perturbed with a precession frequency $\omega R_{jt}/u = 0.1$ (a period of about 840 years) shown in Figure 8. This volumetric rendering of $\rho^2 T$ at an angle of inclination of 45° is at simulation time $\tau_{sym} = 100$ (a time of about 6700 years). In the simulation the linear scale of the knot forming region is $< 100R_{jt}$ ($< 0.1 \text{ pc}$). In the simulation the “hot spots” occur at the intersections of helical surface and body waves. The intersections interact with the external medium and are shocked as the jet moves supersonically through the ambient gas, and shock spurs develop in Figure 8 at knots farther from the origin. Hot spots closer to the nozzle are relatively “younger” and are just formed. When a hot spot is newly formed as a result of wave-wave interaction it should be nearly stationary. However, the hot spot material moves with the jet flow and generates a strong shock at the jet-ambient interface (the shock spurs in Figure 8) the material behind the shock spur should have a velocity of about 1/4 of the shock speed (also about 1/4 the jet speed). Observed emission should come from the higher temperature shocked material at the jet ambient interface. As time passes, the knot is accelerated by the jet and the gas in the knot mixes with the jet gas. Thus, an observation should show that a knot which is closer to the nozzle has lower velocity, and knots farther from the nozzle, i.e., accelerated by the jet, should move faster. Note also that some “hot spots” are on the far side the jet beam, which, as the helical wave develops, move away from us along the line of sight with respect to the jet beam while other hot spots are on the near side of the jet beam and move toward us along the line of sight relative to the jet beam. This mechanism provides additional cyclic variation in the radial velocity of knots.

The initial transverse velocity perturbations used in our simulation are quite small and cannot account for the large velocity variation among the knots observed in HH 83. However, the effect would be larger if the initial perturbation had a considerable amplitude. The termination of the observed jet after knot J would result from disruption of the jet beam. Further downstream, the interaction of the jet material with ambient gas would form the classic bow shock – structure associated with the working surface observed in many HH objects. Because the morphology of the source and of the simulation are very similar we believe that we have found a mechanism that could result in variation or systematic increase in radial velocity of knots.

Another example of similarity between observational morphology and our simulations is provided by the structure of the jet in HH 111. In particular, the [S II] images of the jet reveal a spiral emission feature wrapped around the jet beam with embedded knots, and the H_α images

present us with remarkable staggered bow shocks farther out along the jet beam (Reipurth et al. 1997). We can immediately identify the spiral emission feature and bright knots with features like those seen in the Mach 5 DM cooling jet perturbed with a precession frequency of $\omega R_{jt}/u = 0.4$ (a precession period of about 210 years) or with the Mach 20 DM cooling jet (jet speed of 236 km s⁻¹) perturbed with a precession frequency of $\omega R_{jt}/u = 1$ (a precession period of about 21 years). Volumetric rendering of $\rho^2 T$ of the Mach 5 and Mach 20 simulations are shown in Figures 5 & 11, respectively. In particular, helical emission bands and the knots seen in the Mach 20 simulation and in the [S II] map from Reipurth et al. (1997) have wavelength and spacing relative to the jet radius that is similar in both the simulation and the observed jet. That this type of structure appears in both simulations at very different precession periods and jet velocities suggests that no fine tuning is required to generate such structure. Because of the limited domain size in the Mach 20 simulation, we do not know whether the observed staggered bow shock can be formed at larger distance. However, the Mach 5 simulation that develops faster spatially suggests that this would be so.

PEH acknowledges support from the National Science Foundation through grant AST-9802955 to the University of Alabama. JMS acknowledges support from DOE grant DFG0398DP00215 to the University of Maryland.

REFERENCES

- Bassett, G.M., & Woodward, P.R. 1995, *ApJ*, 441, 582
- Birkinshaw, M. 1991, in *Beams and Jets in Astrophysics*, ed. P. Hughes, (Cambridge: CUP), 278
- Biro, S. 1996, *MNRAS*, 278, 990
- Biro, S., & Raga, A. 1994, *ApJ*, 434, 221
- Blondin, J.M., Fryxell, B.A., & Königl, A. 1990, *ApJ*, 360, 370
- Bodo, G., Massaglia, S., Ferrari, A., Trussoni, E. 1994, *A&A*, 283, 655
- Bührke, T., Mundt, R., & Ray, T.P. 1988, *A&A*, 200, 99
- Burrows, C. et al. 1996, *ApJ*, 473, 437
- Cernicharo, J., & Reiputh, B. 1996, *ApJ*, 460, L57
- Curiel, S. 1995, *Rev. Mex. Astr. Ap. Serie de Conferencias*, 1, 59
- Dalgarno, A., & McCray, R.A. 1972, *ARA&A*, 10, 375 (DM)
- Downes, T.P., & Ray, T.P., 1998, *A&A*, 331, 1130
- de Gouveia dal Pino, E.M., & Benz, W. 1993, *ApJ*, 410, 686
- de Gouveia dal Pino, E.M., & Benz, W. 1994, *ApJ*, 435, 261
- Eislöffel, J., & Mundt, R., 1995, *Ap&SS*, 233, 55
- Falle, S.A.E.G., Innes, D.E., Wilson, M.J. 1987, *MNRAS*, 225, 741
- Graham, J., & Elias, J.H. 1983, *ApJ*, 272, 615
- Hardee, P.E. 1983, *ApJ*, 269, 94
- Hardee, P.E. 2000, *ApJ*, 533, in press
- Hardee, P.E., & Clarke, D.A. 1995, *ApJ*, 451, L25
- Hardee, P.E., Clarke, D.A., & Rosen, A. 1997, *ApJ*, 485, 533 (HCR)
- Hardee, P.E., Cooper, M.A., & Clarke, D.A. 1994, *ApJ*, 424, 126
- Hardee, P.E., & Norman, M.L. 1988, *ApJ*, 334, 70
- Hardee, P.E., Rosen, A., Hughes, P.A., & Duncan, G.C. 1998, *ApJ*, 500, 599
- Hardee, P.E., & Stone, J.M. 1997, *ApJ*, 483, 121
- Hunter, J.H., & Whitaker, R.W. 1989, *ApJS*, 71, 777
- Keppens, R. & Tóth, G. 1999, *Phys. of Plasmas*, vol.6, no.5, 1461

- Loken, C., Burns, J., Bryan, G., & Norman, M.L. 1996, in A.S.P. Conference Proceedings Volume 100: Energy Transport in Extragalactic Radio sources and Quasars, eds, P. Hardee, A. Bridle, & A. Zensus (San Francisco: ASP), 267
- MacDonald, J., & Bailey, M.E. 1981, MNRAS, 197, 995 (MB)
- Marti, J., Rodriguez, L.F., & Reipurth, B. 1995, ApJ, 449, 184
- Mundt, R., Brugel, E.W., Bührke, T. 1987, ApJ, 319, 275
- Mundt, R., Bührke, T., Fried, J.W., Neckel, T., Sarcander, M., Stocke, J. 1984, A&A, 140, 17
- Nagar, N.M., Vogel, S.N., Stone, J.M., & Ostriker, E.C. 1997, ApJ, 482, L195
- Norman, M.L., & Hardee, P.E. 1988, ApJ, 334, 80
- Ray, T.P. 1987, A&A, 171, 145
- Ray, T.P. 1997, Proceedings of the NATO ASI on Solar and Astrophysical MHD Flows, Heraklion, ed. K. Tsinganos, Kluwer Acad. Pub.
- Ray, T.P., & Mundt, R. 1993, in Astrophysical Jets, eds. M. Fall, C. O’Dea, M. Livio and D. Burgarella, (Cambridge University Press), p145
- Raga, A.C., & Kofman, L. 1992, ApJ, 386,222
- Reipurth, B. 1989, A&A, 220, 249
- Reipurth, B., Bally, J., Graham, J.A., Lane, A.P., Zealey, W.J. 1986, A&A. 164, 51
- Reipurth, B. & Cernicharo, J. 1995, Rev. Mex. Astr. Ap. Serie de Conferencias, 1, p43
- Reipurth, B., Hartigan, P., Heathcote, S., Morse, J. & Bally, J. 1997, AJ, 114,757
- Rossi, P., Bodo, G., Massaglia, S., & Ferrari, A., 1997, A&A, 321, 672
- Suttner, G., Smith, M.D., Yorke, H.W., & Zinnecker, H., 1997, A&A, 318, 595
- Stone, J.M., Xu, J.J., & Hardee, P.E. 1997, ApJ, 483, 136
- Stone, J.M., & Norman, M.L. 1993a, ApJ, 413, 198
- Stone, J.M., & Norman, M.L. 1993b, ApJ, 413, 210
- Stone, J.M., & Norman, M.L. 1994, ApJ, 420, 237
- Strom, K.M, Strom, S.E., Wolff, S.C, Morgan, J., Wenz, M. 1986, ApJS, 62, 39

Table 1: Physical and numerical parameters used in 3D simulations.

Mach #	Type ¹	Grid	z/R_{jt}	$(xy)/R_{jt}$	$\omega R_{jt}/u$	$\theta(rad)$	XYZones/ R_{jt}	τ_{sim}
20	A,D	$200 \times 80 \times 80$	500	± 4	0.025	0.0025	12	25
20	D	$100 \times 80 \times 80$	60	± 4	1.0	0.01	10	5
5	D	$200 \times 94 \times 94$	400	± 8	0.1	0.0075	10	100
5	A,D,M	$200 \times 80 \times 80$	60	± 4	0.4	0.03	10	15
5	A,D,M	$200 \times 120 \times 120$	300	± 10	1.0	0.075	6	80

¹ Cooling type – A: Adiabatic, D: DM cooling, and M: MB cooling

Table 2: Growth rates of surface modes for Mach 5 jets precessed at $\omega R_{jt}/u = 0.4$

Mode	$k_I R_{jt}$ (AD)	$k_I R_{jt}$ (DM)	$k_I R_{jt}$ (MB)	$2\pi/k_I$ (AD)	$2\pi/k_I$ (DM)	$2\pi/k_I$ (MB)
Helical ¹	-0.062	-0.087	-0.068	$101R_{jt}$	$72R_{jt}$	$92R_{jt}$
Elliptical ²	-0.135	-0.273	-0.131	$46R_{jt}$	$23R_{jt}$	$48R_{jt}$
Triangular ²	-0.229	-0.274	-0.210	$27R_{jt}$	$23R_{jt}$	$30R_{jt}$
Rectangular ²	-0.336	-0.327	-0.303	$18R_{jt}$	$19R_{jt}$	$21R_{jt}$

¹ Growth rate at precession frequency $\omega R_{jt}/u = 0.4$

² Maximum growth rate

Table 3: Helical S, B1 & B2 modes on jets precessed at $\omega R_{jt}/u = 1.0$

Type	$k_R R_{jt}$ (S)	$k_R R_{jt}$ (B1)	$k_R R_{jt}$ (B2)	$\Delta k_R R_{jt}^1$	$k_I R_{jt}$ (S)	$k_I R_{jt}$ (B1)	$k_I R_{jt}$ (B2)
Mach 5 Jets							
AD	—	1.30	1.46	0.16	—	-0.072	-0.054
DM	—	1.18	1.42	0.24	—	-0.043	-0.025
MB	—	1.30	1.44	0.14	—	-0.080	-0.032
Mach 20 Jet							
DM	1.3059	1.0339	1.0868	0.0529	-0.0572	-0.0012	-0.0035

¹ $[\Delta k_R R_{jt} = k_R R_{jt} (B2) - k_R R_{jt} (B1)]$

7. Figures

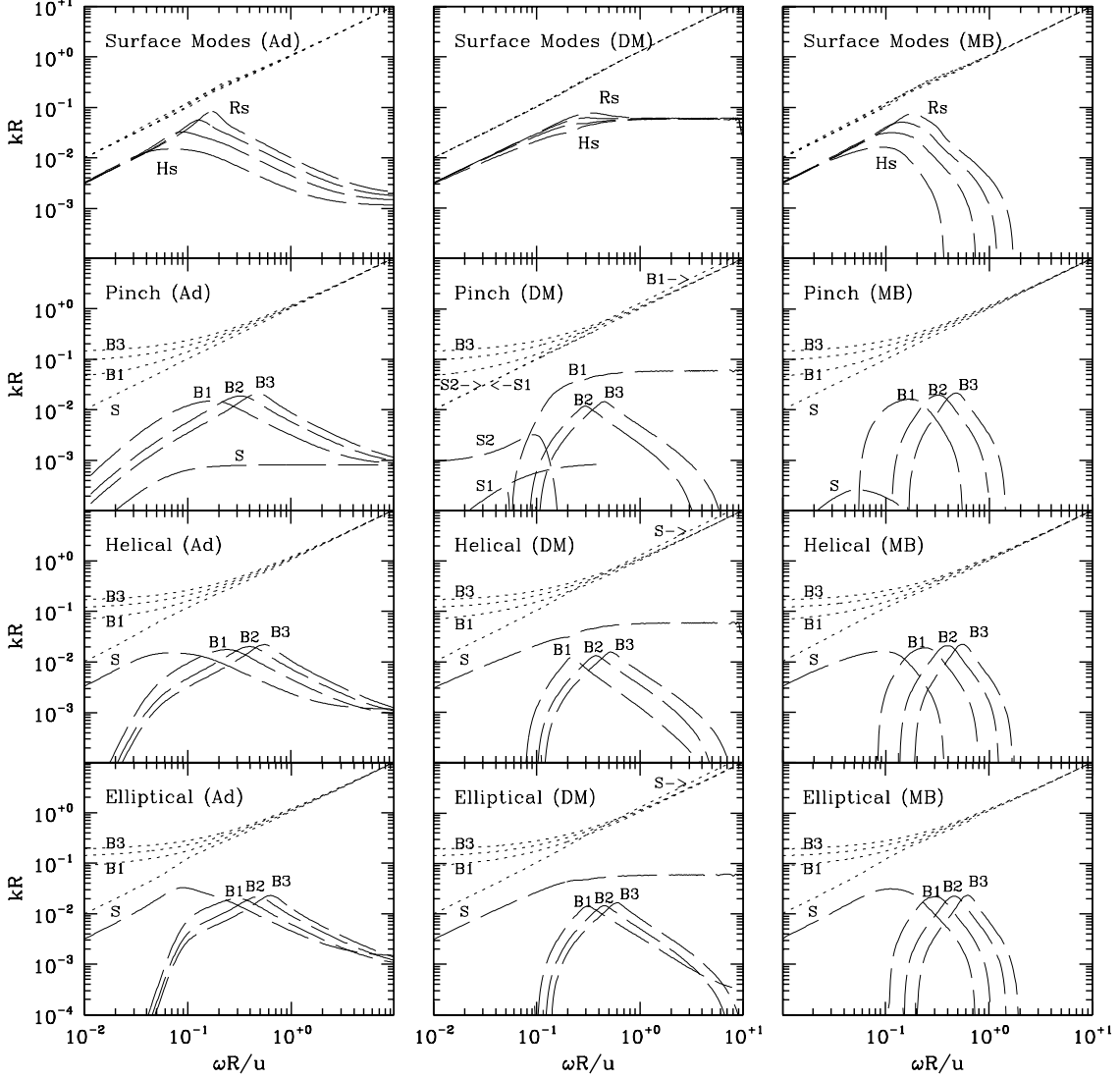


Fig. 1—Surface wave solutions to the dispersion relation for the helical (Hs), elliptical, triangular and rectangular (Rs) normal modes on the Mach 20 Ad(iabatic), DM cooling and MB cooling jets (top panels). Surface (S) wave solutions and first three body wave (B1, B2, B3) solutions to the dispersion relation for the pinch, helical and elliptical normal modes on the Mach 20 Ad(iabatic), DM cooling and MB cooling jets (lower panels). The dotted lines give the real part of the wavenumber, k_R , and the dashed lines give the absolute value of the imaginary part of the wavenumber, $|k_I|$, as a function of the angular frequency, ω . Quantities are scaled by the jet radius, R_{jt} , and the jet velocity, u .

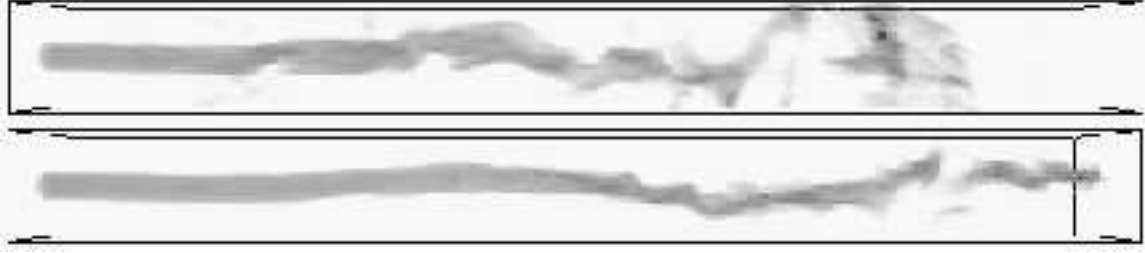


Fig. 2—Volumetric rendering of density for the Mach 20 DM jet (top) and Adiabatic jet (bottom) with $\omega R_{jt}/u = 0.025$. The volume shown is $500R_{jt} \times 8R_{jt} \times 8R_{jt}$. The images are underscaled horizontally by a factor six. Darker shading indicates higher density.

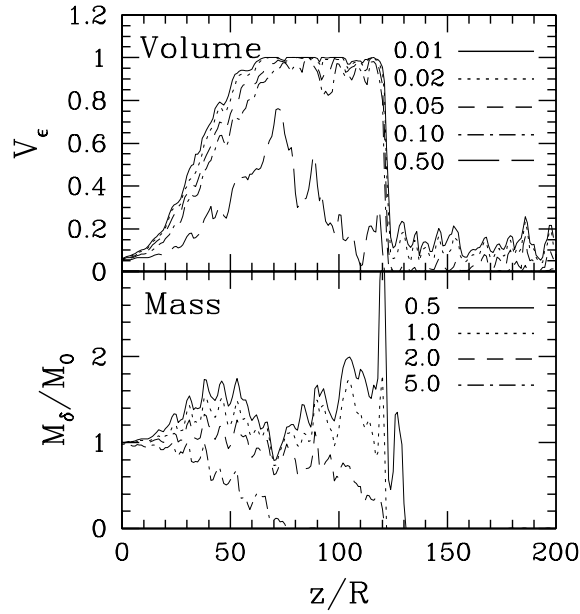


Fig. 3—Entrainment volume V_ϵ (top) and entrained mass M_δ (bottom) vs. axial position for a Mach 5 DM jet with $\omega R_{jt}/u = 0.1$. Lines are at values of $\epsilon = 0.01, 0.02, 0.05, 0.1$ & 0.5 . and $\delta = 0.5, 1, 2$ & 5 .



Fig. 4—Volumetric rendering of temperature (top) and density (bottom) for a Mach 5 DM jet at $\omega R_{jt}/u = 0.4$. The maximum temperature and density are $\approx 40,000$ K and $\approx 1,400$ cm^{-3} , respectively, and the volume shown is $60R_{jt} \times 8R_{jt} \times 8R_{jt}$. Darker shading indicates higher temperature. In general higher densities are darker but in the first half of the jet lighter areas are also above the initial jet density.



Fig. 5—Composite $\rho^2 T$ volumetric rendering of the Mach 5 DM jet at $\omega R_{jt}/u = 0.4$ shown in Figure 4. The jet is inclined at 45° to the line of sight and the volume shown is $60R_{jt} \times 8R_{jt} \times 8R_{jt}$. Darker shading indicates higher values of $\rho^2 T$.

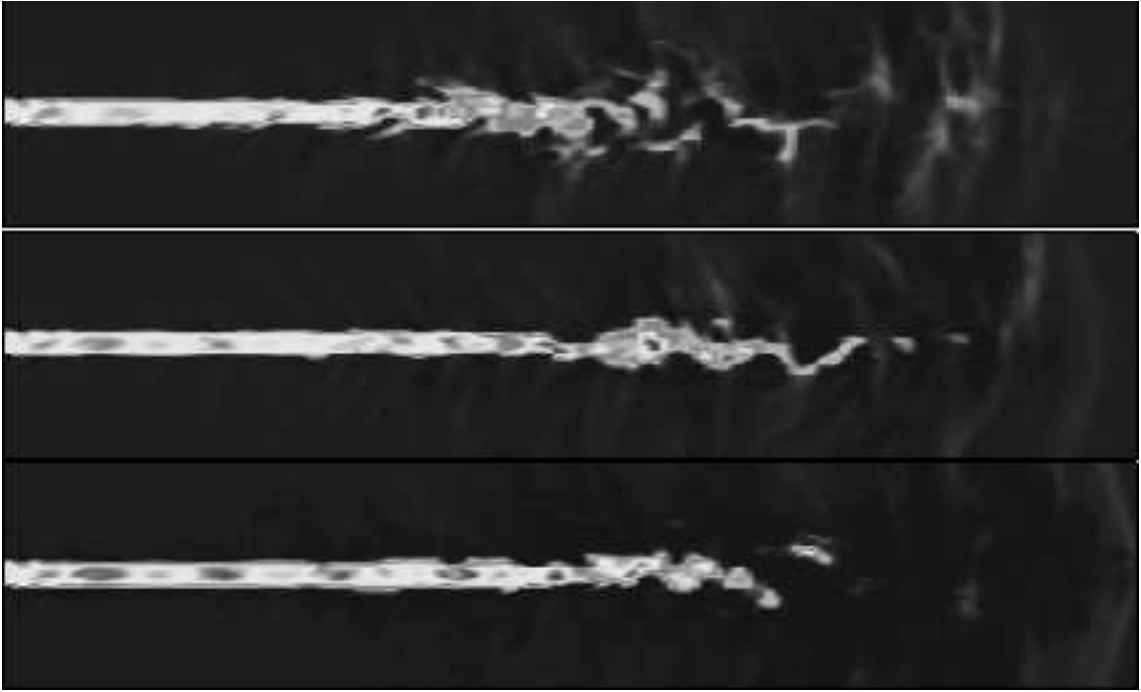


Fig. 6—Center cuts in density of Mach 5 AD (bottom), DM (middle), and MB (top) jets at $\omega R_{jt}/u = 1.0$. Mapping to greyscale is the same in each panel and the panel size is $300R_{jt} \times 20R_{jt}$ and underscaled horizontally by a factor of 3. In general, lighter shading indicates higher density but in the jet the darkest shading indicates the highest densities. Densities range from $\approx 60 \text{ cm}^{-3}$ in the ambient to a maximum of $\approx 1,200 \text{ cm}^{-3}$ in the jet.

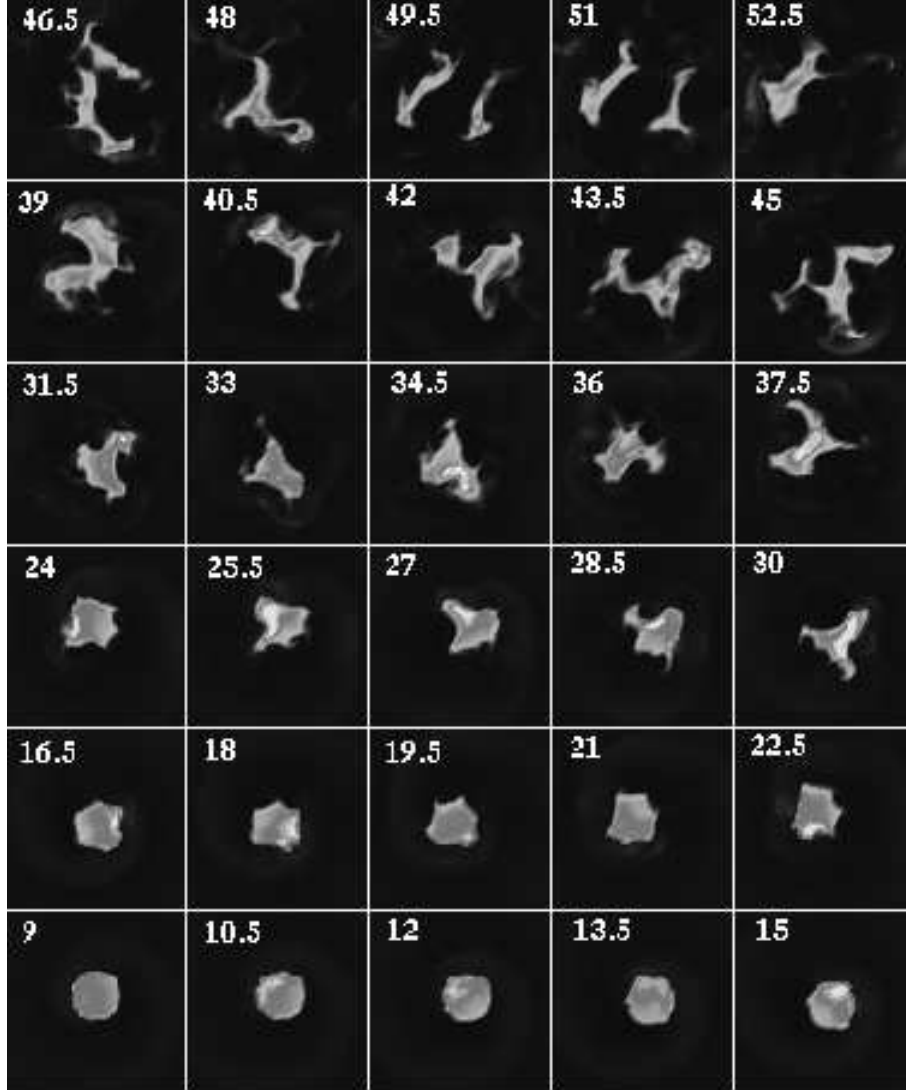


Fig. 7—Mach 5 DM jet cross sections at $\omega R_{jt}/u = 0.4$. The number in each frame indicates the distance from the inlet in units of R_{jt} . In general, a lighter shade in these cross sections indicates a higher density but in the jet the darkest shading within lighter regions indicates the highest densities. Densities range from $\approx 60 \text{ cm}^{-3}$ in the ambient to a maximum of $\approx 1,200 \text{ cm}^{-3}$ in the jet.

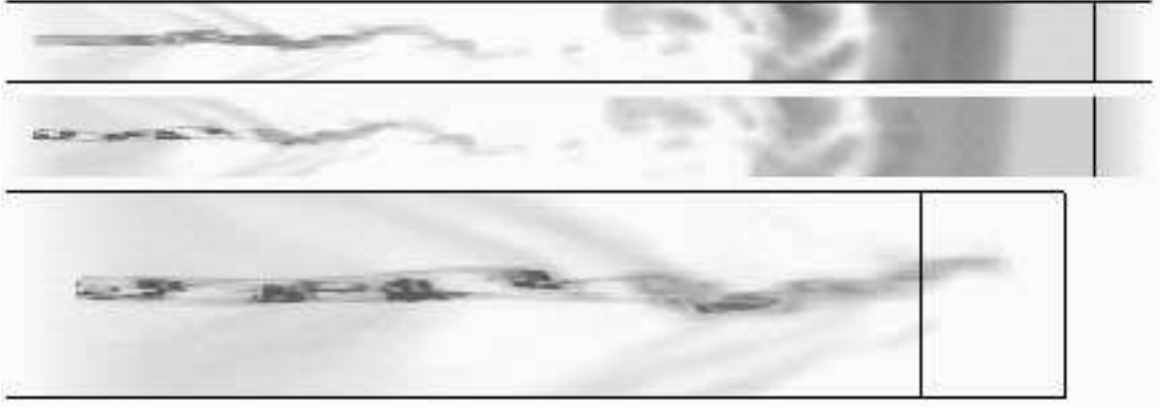


Fig. 8—Composite $\rho^2 T$ volumetric rendering of the Mach 5 DM jet at $\omega R_{jt}/u = 0.1$. The jet is inclined at 45° to the line of sight. Panels show the entire jet (top), and entire jet excluding material with $T < 1000$ K (middle) with volume $300R_{jt} \times 16R_{jt} \times 16R_{jt}$. Lower panel shows the knot region excluding material with $T < 1000$ K with volume $50R_{jt} \times 16R_{jt} \times 16R_{jt}$. Darker shading indicates higher values of $\rho^2 T$ and reveals the hot dense parts of the jet.

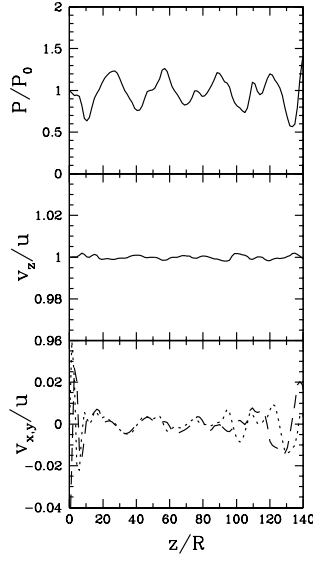


Fig. 9—Plots of pressure (top), axial velocity (middle) and transverse velocity components (bottom) along the jet axis from the Mach 5 DM jet at $\omega R_{jt}/u = 1.0$.

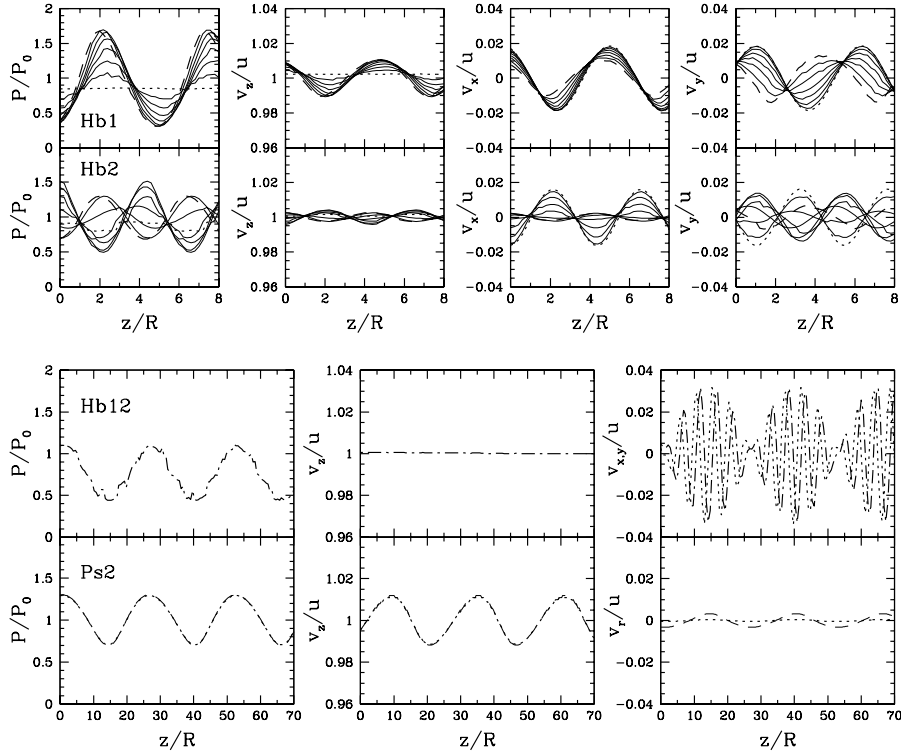


Fig. 10—(top two rows) Pressure, axial velocity (v_z), azimuthal velocity (v_x) and radial velocity (v_y) for the first two helical body modes Hb1 and Hb2 on a Mach 5 DM jet along 1D cuts parallel to the z -axis at radial locations $r/R = 0/8, 1/8, 2/8, \dots, 7/8$ on the $+y$ -axis. The outermost (innermost) radial locations are indicated by the dashed (dotted) lines. (bottom two rows) Pressure, axial velocity (v_z) and transverse velocity components for wave-wave interaction between the two helical body modes (Hb12) along the jet axis, and for the pinch cooling mode (Ps2). For Ps2, v_r is shown on the axis (dotted line) and near to the jet surface (dashed line).

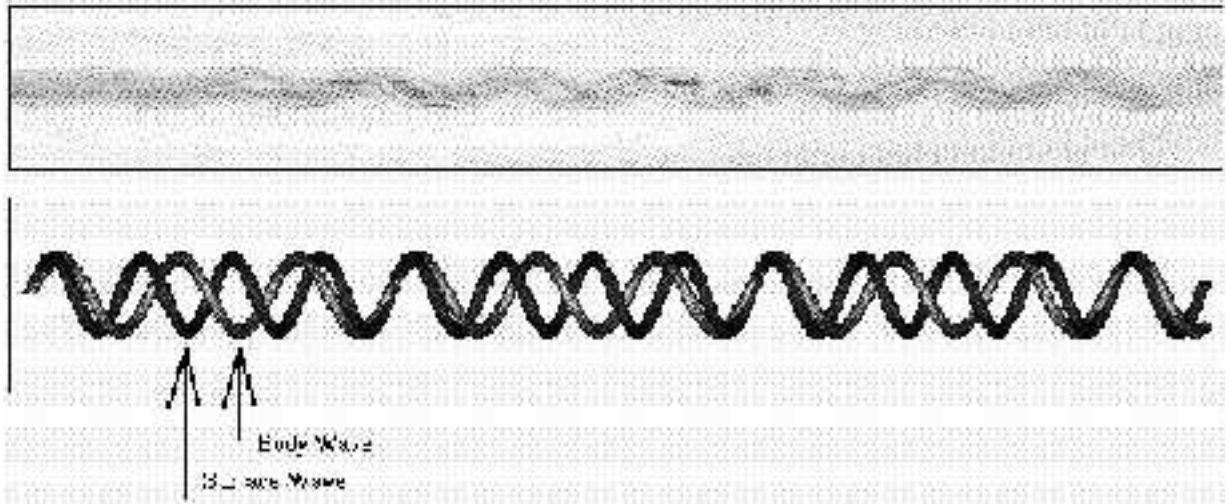


Fig. 11—Composite $\rho^2 T$ volumetric rendering of the Mach 20 DM jet at $\omega R_{jt}/u = 1.0$ (top) and illustration of the interaction between surface and body wave (bottom). The size shown is $60R_{jt} \times 8R_{jt}$. Darker shading in the volumetric rendering indicates higher values of $\rho^2 T$.

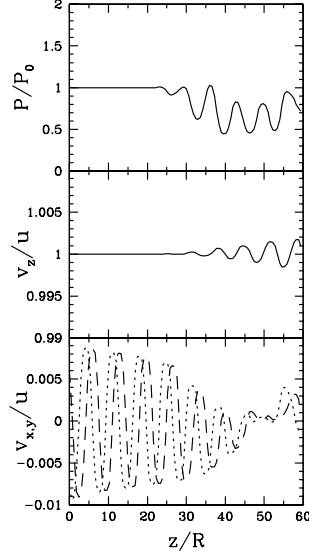


Fig. 12—Plots of pressure (top), axial velocity (middle) and transverse velocity components (bottom) along the jet axis from the Mach 20 DM jet at $\omega R_{jt}/u = 1.0$.

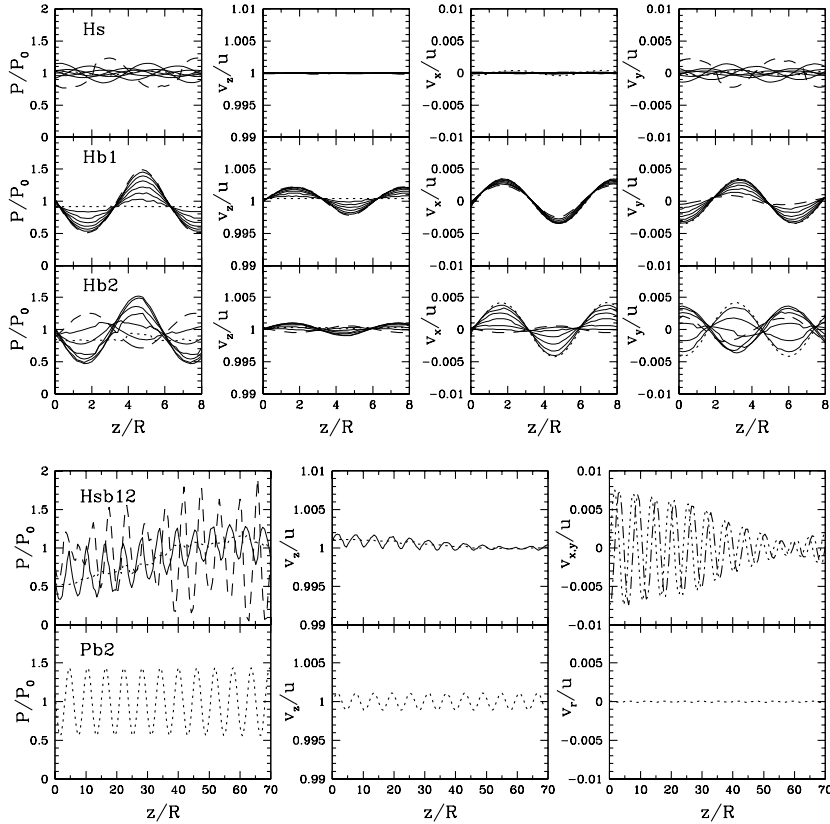


Fig. 13—Similar to Figure 10 but for helical surface (Hs), helical body modes Hb1 and Hb2 and pinch body mode Pb2 on a Mach 20 DM jet. The pressure panel for the combined helical surface and body waves (Hsb12) shows 1D cuts along the jet axis (dotted line), at $r/R = 1/8$ (solid line) and at $r/R = 7/8$ (dashed line). The axial velocity panel shows 1D cuts along the jet axis (dotted

line), at $r/R = 1/8$ (solid line). Pressure, axial velocity (v_z) and radial velocity for the pinch body mode (Pb2) are plotted along the jet axis in the lower panels.